Experimental and computational analysis of vertical jet fires of methane in normal and sub-atmospheric pressures

Rengel B.[1], Àgueda A.[1], Pastor E.[1], Casal J.[1], Planas, E.[1], Hu L.[2], Palacios A.[3,*]

[1]Centre for Technological Risk Studies, Department of Chemical Engineering, Universitat Politècnica de Catalunya, Barcelona, Spain.
[2]State Key Laboratory of Fire Science, University of Science and Technology of China, Hefei, China.
[3]Universidad de las Americas Puebla, Department of Chemical, Food and Environmental Engineering, Puebla, Mexico.
**Corresponding author email: adriana.palacios@udlap.mx*

ABSTRACT

Accidental jet fires occurring in industrial facilities can involve severe consequences as they can trigger domino effect. The assessment of the flame-geometry descriptors of the jet can contribute to prevent flame impingement on plant equipment, hence reducing inventory loss and structural collapse. This paper reports the geometrical features of vertical methane subsonic jet flames at normal and sub-atmospheric pressures: 1.0 atm, 0.9 atm, 0.8 atm, 0.7 atm and 0.6 atm. Differences on flame shape are evaluated, and linear correlations of the main geometrical parameters of interest (i.e. lift-off distance, radiant flame length, and equivalent diameter) are defined as a function of the Reynolds number. Moreover, the predictive capabilities of FDS, FireFOAM and FLACS-Fire codes are assessed when determining the geometrical features of jet fire experiments. Based on a qualitative and a quantitative comparison between simulation results and experimental data, the main strengths and weaknesses of each code are identified. Recommendations on suitable grid sizes are delivered.

KEYWORDS

CFD fire modelling; atmospheric and sub-atmospheric pressures; methane jet fires; flame geometry.

NOMENCLATURE

A	surface of the flame (m^2)
c_p	specific heat of air (kJ/kg·K)
D	diameter (m and mm)
D^*	characteristic fire diameter (m)
FB	fractional bias (-)
g	gravitational acceleration (m/s^2)
H	total jet fire length (m)
I	segmented image (-)
k	turbulent kinetic energy (m^2/s^2)
L	radiant flame length (m)
$\dot{m}$	mass flow rate (kg/s)
M	molecular weight of the fuel (kg/kmol)
n	number of variables (-)
$NMSE$	normalized mean square error (-)
P	pressure (atm)
PC	performance criteria (-)
$\dot{Q}$	heat release rate (kW)
r	stoichiometric coefficient (-)

R	universal gas constant
Re	Reynolds number, $4\dot{m}_{or}/\mu\pi D_{or}$
Re_L	Reynolds number based on D_{or} and S_L, $D_{or}S_L/\nu$
S	lift-off distance (m)
S_L	laminar burning velocity (m/s)
T	temperature (K)
u	gas velocity (m/s)
U^*	dimensionless flow number for choked and unchoked flow (-), see Eq. (6)
$\dot{V}$	volumetric flow rate (Nm^3/s)
X	measured/predicted variable

Greek

α	thermal diffusivity (m^2/s)
γ	isentropic ratio (-)
δ_x	cell size (m)
Δ	LES filter size (m)
Δh_c	heat of combustion (kJ/kg)
ε	turbulent dissipation rate (m^2/s^3)
ρ	density (kg/m^3)
τ_{mix}	mixing time scale (s)
ν	kinematic viscosity (m^2/s)
χ	reacting species fractions (-)

Subscripts

eff	effective
eq	equivalent
f	fuel
F	flame
i	initial stagnation conditions
i, j	coordinates
m	measured
or	orifice
p	predicted
sgs	sub-grid scale
th	threshold
∞	ambient conditions

1. Introduction

Hydrocarbon fires are the most frequent accidents occurring in oil and gas industries [1]. Among the possible fires occurring, pool fires are the most common scenarios arising in process plants (66% of the cases), followed by flash fires (29%) and jet fires (5%) [2]. Despite the lower occurrence of jets compared to other hydrocarbon fires, a sudden ignition of an accidental release of pressurized fuel could generate a serious hazard to industry personnel and to the installation itself [3]. An escalation of the incident, known as domino effect, occurs approximately in the 50% of the registered jet fire accidents, with further inventory loss and structural collapse [4].

In order to prevent most severe effects and consequences in the event of a jet fire, it is essential to assess the likelihood of flames impingement on plant equipment [5]. To that end, the flame-geometry descriptors of jets (Fig. 1) must be estimated according to the fire scenario conditions. These are defined as follows: (i) the radiant flame length, L_F, as the distance from the base of the fire to the tip of the visible flame; (ii) the total flame reach, H_F, as the distance from the exit orifice to the tip of the visible flame; (iii) the flame area, A_F, as the flame surface defined by a given isothermal contour or by the visible flame; (iv) the lift-off distance, S_F, as the distance from the exit orifice to the base of the flame; and (v) the equivalent diameter, D_{eq}, as the mean width occupied by the flame.

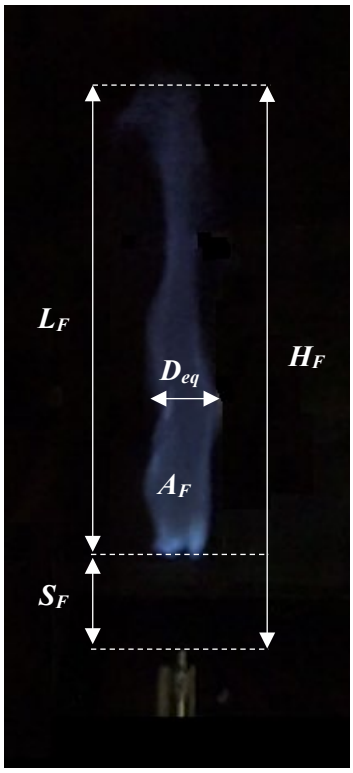

Fig. 1. Flame geometry features of jet fires.

Several experimental studies have been published that provide information on the flame geometry of vertical hydrocarbon jet fires (Table 1). Different fuels, nozzle diameters and flow regimes were studied and most of them were performed at an ambient pressure of 1.0 atm [6–17]. Most of the semi-empirical expressions found in those experiments could be used to assess the risks of accidental jet fires near the sea level; however, these were not initially developed for jet flames at high altitudes.

Variations in the ambient pressure impact on the gaseous fuel density, ρ_f, hence affecting the heat release rate, $\dot{Q} = \rho_f u A_{or} \Delta h_c$, which is defined as one of the most important parameters governing the fire behaviour. Reduced atmospheres, where air is less compressed and lighter, may also alter the chemical reaction of combustion due to the changes on the effective amount of

oxygen available in the ambient air, $O_{2,eff}$. Consequently, fewer molecules of oxygen are present in a volume of air to be mixed with the released fuel.

Table 1. Experimental studies of vertical hydrocarbon jet fires.

Year	Ref.	Fuel	D_{or} (mm)	P_∞ (atm)	Flow Regime
1983	[6]	CH_4	4 - 12	1.0	Subsonic
1984	[7]	CH_4 - C_3H_8	10 - 80	1.0	Subsonic
1986	[8]	CH_4	76 - 102	1.0	Sonic
1989	[9]	CH_4	38 - 102	1.0	Subsonic - Sonic
1994	[10]	C_3H_8	0.84 - 2.58	1.0	Subsonic
1997	[11]	C_3H_8	6.5 - 27.6	1.0	Subsonic
2004-2005	[12,13]	CH_4 - C_3H_8 - C_2H_4	5 - 8	1.0	Subsonic
2007	[14]	C_4H_{10}	2.2	1.0	Subsonic
2009-2012	[15–17]	C_3H_8	10 - 43.1	1.0	Subsonic - Sonic
2013-2015	[18–21]	C_3H_8	4 - 10	0.6 - 1.0	Subsonic
2013	[22]	CH_4	3	0.4 - 1.0	Subsonic
2014	[23]	C_3H_8	4 - 6	0.6 - 1.0	Subsonic
2019	[24]	C_3H_8	0.22	0.5 - 5.5	Subsonic

In case of accident, jet fires at normal atmospheric pressures may be present in offshore platforms, in marine gas and oil fields, and in many liquefied natural gas terminals (i.e. Troll A platform, Norway [25]; Blake oil field, UK [26]; LNG terminal on Maasvlakte, The Netherlands [27]). However, oil and gas fields, gas power plants and refineries can be located at elevated areas, and the pipelines network can cross high altitude regions (i.e. the Permian Basin oil field at 800 m a.s.l. (USA) [28]; the F'Kirina gas power plant at 950 m a.s.l (Algeria) [29]; and the A13 oil pipeline Teheran-Trabniz at a maximum altitude of 2890 m a.s.l. (Iran). Thus, fire behaviour research has to be addressed to check fire protection requirements under sub-atmospheric pressures.

The U.S. Energy Information Administration (EIA) reported that methane gas is one of the most processed, transported and used hydrocarbon fuels these days (Fig. 2) [30]. Nevertheless, jet fires of methane at sub-atmospheric pressures have been barely studied. Therefore, jet fire events at pressures lower than 1.0 atm have to be studied because they represent a possible hazardous scenario in the industrial sector. In particular, the assessment of the flame shape and size of methane jets at different ambient pressures becomes essential to ensure fire safety.

Computational Fluid Dynamics (CFD) models can be used to assess the flame-geometry descriptors of methane jet fires at different ambient pressures. During the last years, CFD modelling has been considerably used in the field of fire risk analysis due to the need for an in-depth understanding of the phenomena associated to hydrocarbon fires [31–35]. CFD tools solve the fundamental conservation equations for mass, momentum, energy and species transport. These are coupled with additional sub-models and parameters, which are commonly defined by default within the codes, to account for the physical and chemical processes in a fire event, i.e. turbulence, combustion and radiation. However, to reduce the uncertainties generated either in the conceptual modelling or during the computational design phase and thus, to increase the

prediction accuracy, CFD validation analyses through sound and comprehensive experimental benchmark data are needed [36].

This paper is aimed at: (i) determining geometry-flame descriptors of vertical subsonic jet fires of methane in normal and sub-atmospheric pressures; (ii) validating the predictive capabilities of three CFD codes when modelling this type of fires. To that end, laboratory-scale methane jet flame tests were performed at different atmospheric pressures: 0.6 atm, 0.7 atm, 0.8 atm, 0.9 atm, and 1.0 atm. Mathematical correlations describing the flame shape were obtained as a function of the Reynolds number. Afterwards, geometry-flame estimations obtained with the computational simulations carried out with FDS, FireFOAM and FLACS-Fire were compared against the experimental results. Four grid sizes were proposed to determine the most suitable grid resolution for each code. Recommendations are delivered based on the agreements found when comparing simulation results against experimental data.

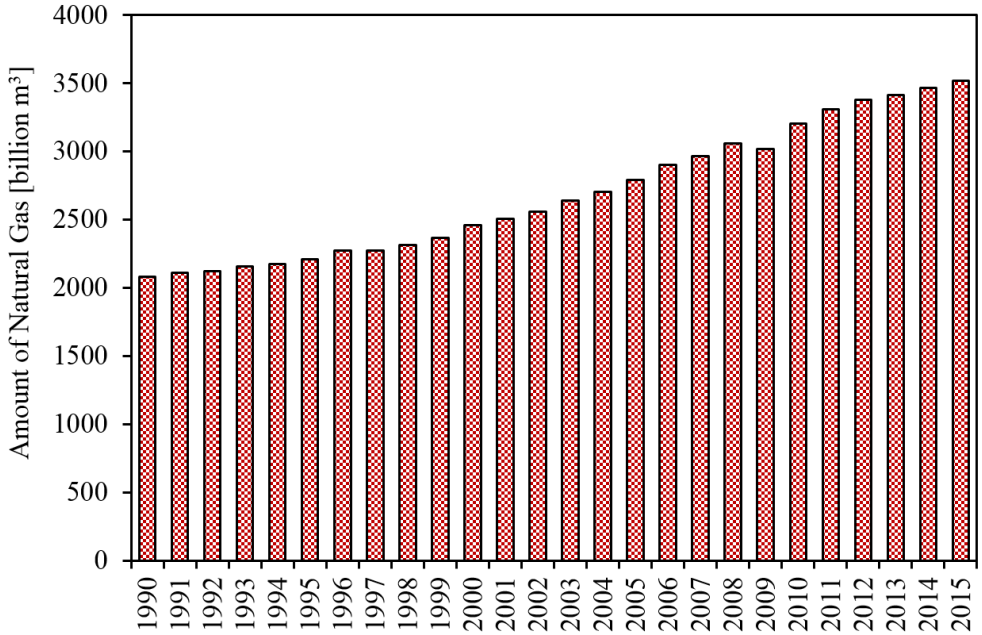

Fig. 2. Evolution of the natural gas production worldwide since 1990 until 2015 [30].

2. Experimental dataset

Vertical subsonic jet fire tests of methane were carried out to determine the geometrical characteristics of the flames at normal and sub-atmospheric pressures: 1.0 atm, 0.9 atm, 0.8 atm, 0.7 atm and 0.6 atm (Table 2). Figure 3 depicts an outline of the experimental facility and measurement setup used for the fire tests. The experimental set-up consisted of a flow supply system, with a 2 m long pipe, a stainless nozzle, and a low air pressure chamber of 3 m (width) x 2 m (length) x 2 m (height). The following parameters were the same for all the tests: an ambient temperature of 25 ºC, a relative humidity of 35%, a constant volumetric methane flow rate of $\dot{V}_{or} = 1.71 \cdot 10^{-4}\, Nm^3/s$, and a nozzle diameter of 3 mm. The fuel supply rates and hence fuel jet exit velocities at the nozzle were controlled through the flow rate meter.

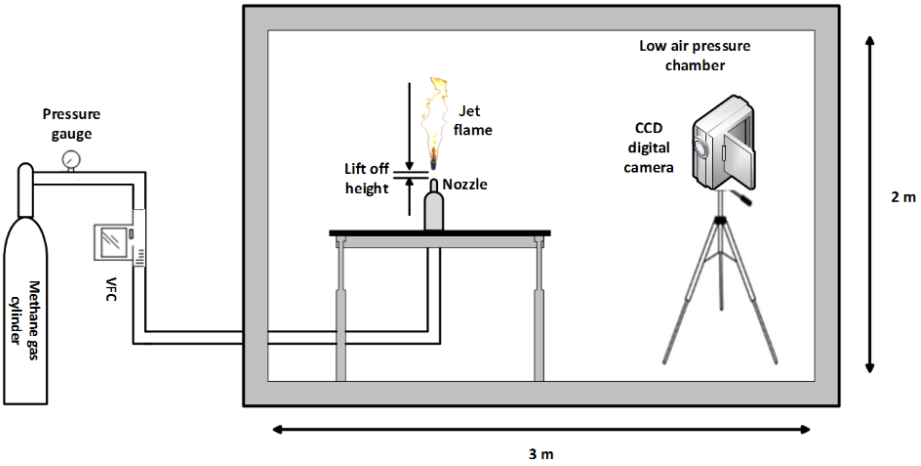

Fig. 3. Experimental facility for the study of turbulent and vertical methane jet fires at normal and sub-atmospheric pressures. VFC stands for volume flow controller, and CCD for charged-coupled device.

The ambient pressure inside the chamber was regulated and maintained by a vacuum pump, and controlled by a pressure sensor. As the ambient pressure decreased, other parameters affecting the jet fires development also decreased: the amount of oxygen per unit volume [37], $O_{2,eff}$, the fuel density expressed as $\rho_f = P_\infty M/RT_\infty$, the mass flow rate of the gas released through the orifice, $\dot{m}_{or} = \rho_f \dot{V}_{or}$, and the Reynolds number, $Re = 4\dot{m}_{or}/\mu\pi D_{or}$. Each test began when the pressure inside the chamber was stable for a period of about 5 min after pumping fresh air into the low pressure chamber to replace previous air. The duration of each experimental test was 2 min.

Table 2. Turbulent vertical methane jet fire experiments dataset (orifice diameter = 3 mm).

Experiment	P_∞ (atm)	$O_{2,eff}$	ρ_f (kg/m^3)	$\dot{m}_{or}$ (kg/s)	Re
1	0.6	0.12	0.39	$6.7\cdot10^{-5}$	$2.6\cdot10^{3}$
2	0.7	0.14	0.46	$7.8\cdot10^{-5}$	$3.0\cdot10^{3}$
3	0.8	0.16	0.52	$8.9\cdot10^{-5}$	$3.5\cdot10^{3}$
4	0.9	0.18	0.59	$1.0\cdot10^{-4}$	$3.9\cdot10^{3}$
5	1.0	0.21	0.66	$1.1\cdot10^{-4}$	$4.3\cdot10^{3}$

A charged-coupled device (CCD) digital camera of sensor size 8.5 mm and an image size of 320 x 240 pixels was used to film the jet fire experiments. The recording frequency was 25 Hz. For each video footage, an image segmentation process was performed to discriminate the flame region from the background and to determine the flame-geometry descriptors of the jet fires. Figure 4 shows the main steps followed to segment the images with the Interactive Segmentation Tool® [38]. First, the frames belonging to the steady state were extracted each at a rate of 2 Hz and individually imported (Step 1). Then, for each image, a red continuous line was manually drawn to define the flame contour (Step 2).

Following, an outer contour was also drawn within the background of the image in a blue continuous line to facilitate the colour distinction between the flame and the rest of the picture (Step 3). Automatically, the Binary Partition Trees algorithm [39] was applied to segment the image and save it as a binary file (Step 4). It transforms a hierarchical region segmentation into an object-background segmentation by using the user interactions to split and merge regions. After that, the ImageJ® software [40] was used to convert the binary files created into spreadsheet documents containing a binary matrix, where 0 corresponds to background regions and 1 to flame regions. Based on the exit orifice diameter and the dimensions of the imported image, the flame-geometry descriptors were determined for the complete set of segmented images.

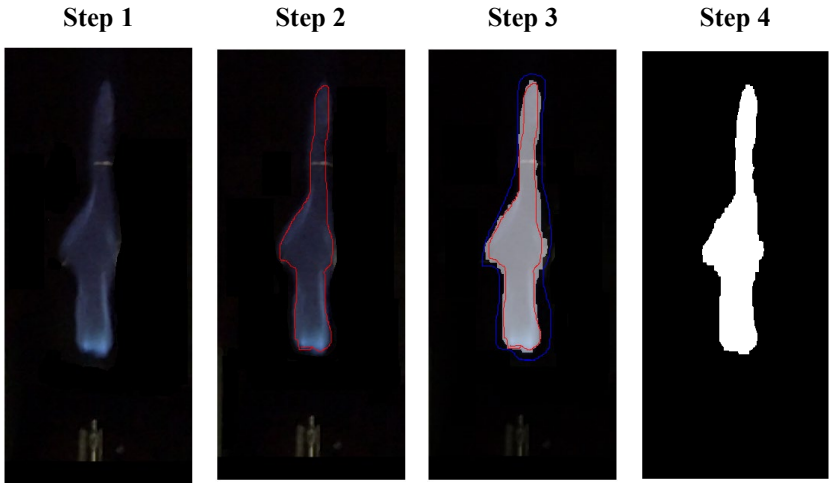

Fig. 4. Instant captures of a test (atmospheric pressure = 0.7 atm) in the steady state. The four steps followed during the image segmentation process are depicted. Red line depicts the manually drawn flame contour. Blue line depicts the outer contour.

3. Computational fluid dynamics

Three CFD codes were used to simulate the methane jet fire experiments: Fire Dynamics Simulation v6.7.0 (FDS) [41], the fire solver of OpenFOAM v6 (FireFOAM) [42], and the Flame Acceleration Simulator v10.7 (FLACS-Fire) [43]. FDS is an open source code developed by the NIST (National Institute of Standards and Technology) that numerically solves a form of the Navier-Stokes equations appropriate for low-speed, thermally-driven flows. FireFOAM is another open code developed by the firms CFD Direct and FM Global. It is based on a set of object-oriented CFD toolboxes written in C++. Both codes, FDS and FireFOAM, are able to perform fire simulations under multiple grids, which can be of high interest: (i) when high resolution is required to simulate complex obstructions present within the computational domain, and (ii) to split the modelled volume into several grids of different sizes to speed up the computational times. FLACS-Fire is a commercial CFD code (Gexcon AS) especially designed for fire hazards applications in industries. With FLACS-Fire, one mesh can be modelled with stretching capabilities.

In FDS and FireFOAM, the stability criteria in the explicit schemes is regulated through the Courant-Friedrichs-Lewy (CFL) condition, which places a restriction on the time step to maintain physically realizable conditions. In both codes, a default CFL value of 0.8 was defined to avoid a fluid element to traverse more than one cell within a time step; hence keeping the implicit temporal and spatial filters consistent with the LES turbulence approach. On the other hand, the time stepping scheme in FLACS-Fire relies on the CFL numbers based on the speed of sound (CFLC) and flow velocity (CFLV). As recommended in the user's guide [43], a CFLC of 20 and a CFLV of 2 were set-up for the fire simulations regardless of the cell size defined. Additional information on the numerical schemes used in the codes can be found in Rengel et al. [44] for FDS and FLACS-Fire, and in Maragkos et al. [45] for FireFOAM.

Simulations lasted 30 s and fire scenario conditions (i.e. mass flow rates, ambient temperature, pressure, and humidity) were prescribed according to the experimental set-up. The Conversion Factor Model (CFM) was used in the codes to directly convert a certain fraction of the fuel carbon to soot. For methane jet fires, a soot yield of 0.7 % was prescribed as the fraction of carbon from the fuel converted to soot [46]. However, an analysis about the effect of soot yield fraction on flame geometry results has also been performed and reported in section 4.2.3.

In the following sub-sections turbulence and combustion models used in the codes are described and cell sizes criteria and simulation outputs are defined. It is worth noting that radiation was not solved in any code, as it has a negligible impact on the flame geometry.

3.1. Turbulence modelling

The exact solution of the governing equations is beyond the capabilities of the most powerful computers due to the high-turbulent flows occurring in large-scale fires. Alternatively, the flow structures can be modelled using a sub-grid scale (SGS), sufficiently small to account for all relevant, significant processes. In order to diminish the possible uncertainties derived from the SGS modelling, numerous turbulence sub-models have been developed and implemented in CFD codes.

In the case of FLACS-Fire, the Reynolds Averaged Navier-Stokes (RANS) model is applied [47], whereas FDS and FireFOAM represent the flow motion by means of the Large Eddy Simulations (LES) approach [48]. The former is the less expensive model as it solves the Navier-Stokes equations for the mean flow variables. In FLACS-Fire, to solve the equations closure problem, the $k-\varepsilon$ two-equation eddy viscosity model is implemented, where k represents the turbulent kinetic energy and ε the dissipation rateDue to the use of temporary averages, the RANS method usually does not allow a good temporary resolution of the system, but can provide a good spatial resolution.

LES is not a time average approach such as RANS. In LES, the way of resolving turbulence to reduce the computational cost is to ignore what is happening on the smaller scales. A temporal and spatial filtering of the Navier-Stokes equations is made to eliminate the information contained in the smaller scales. This information, however is not irrelevant and it is necessary to model it in some way, especially in those cases where small scale events can be important (fluxes near walls, with chemical reaction, etc.). To solve this LES requires what are called sub-grid scale models (SGS), which require empirical information. LES is more computational expensive and more grid sensitive; non-reliable results can be obtained if there are not enough cells to describe the flow field [49]. FDS and FireFOAM dynamically solve the turbulence as a function of the sub-kinetic energy, the LES filter size (i.e. cubic root of the cell volume), and the Smagorinsky constant.

3.2. Combustion modelling

In all the codes, the Eddy Dissipation Concept (EDC) was the approach used to simulate the interaction between the turbulent flow and the chemical reactions [50]. This is an appropriate model when the detailed kinetics of the fuel are not important and when the products of combustion released are known from experimental data [49]. Within this framework, the 'mixed is burnt' assumption is considered, hence neglecting the chemical kinetic effects. Therefore, the reaction of fuel species and air occurs immediately when fuel and air are available in a cell.

The chemistry is simplified and it is only necessary to calculate mixing time scales, τ_{mix}, which dictate the required time to carry out the mixture between the fuel and the oxidizer [51]. Indeed, the main difference between codes using the EDC approach lies on the way they deal with the mixing time scales. For example, mixing time scales in FLACS-Fire are expressed as follows:

$$\tau_{mix} = \frac{2.433\left(\frac{\varepsilon}{\nu}\right)^{1/2}\gamma^3\chi}{1-\gamma^3\chi} \quad (1)$$

where ε represents the dissipation rate, ν the kinematic viscosity, χ the reacting species fractions, and γ the isentropic ratio, determined as:

$$\gamma = min\left(0.8, 2.13\left(\frac{\nu\varepsilon}{k^2}\right)^{1/4}\right) \quad (2)$$

where k is the turbulent kinetic energy.

In FireFOAM, the mixing scale time depends on model constants, the LES filter size (Δ) and the sub-grid kinetic energy (k_{sgs}) as follows [52]:

$$\tau_{mix} = \frac{\Delta}{4.192 k_{sgs}^{1/2}} \quad (3)$$

On the other hand, FDS uses the most detailed mixing time scale model, based on the fastest physical process of the local state of the flow field [53]:

$$\tau_{mix} = max\left[10^{-4}, min\left(\frac{\Delta^2}{\alpha}, \frac{0.4\Delta}{\sqrt{\left(\frac{2}{3}\right)k_{sgs}}}, \sqrt{\frac{2\Delta}{g}}\right)\right] \quad (4)$$

where α is the thermal diffusivity.

Within the simple combustion model solved, the gas fuel molecules (carbon, C, hydrogen, H, oxygen, O, and nitrogen, N) react with air to form the products of combustion defined by default (H_2O, CO_2, soot, N_2, and CO) as follows:

$$C_x H_y O_z N_v + r_{air} Air \rightarrow r_{CO_2} CO_2 + r_{H_2O} H_2O + r_{CO} CO + r_s Soot + r_{N_2} N_2 \quad (5)$$

where r represents the stoichiometric coefficients of the species. In particular, stoichiometric coefficients are automatically calculated for H_2O, CO_2, and N_2, while they are user-defined as input data for soot and CO yields.

3.3. Cell size and computational domain

Accuracy of computational models greatly depends on the grid size, which probably represents the most important parameter defined by the user in CFD fire simulations. Besides, the computational time will also depend on the mesh resolution: the thinner the cell size, the better the computational resolution and the greater the simulation time [54]. Therefore, it is necessary to provide a good balance between low grid resolution and reasonable computational costs.

The selection of suitable cell sizes mostly depends on the fire regime. Based on a vast data bank covering 880 sets of jet flames, Bradley et al. [55] identified the flow regime as a function of a dimensionless flow number for choked and unchoked flow, U^*:

$$U^* = \left(\frac{u_f}{S_L}\right) Re_L^{-0.4} \left(\frac{P_i}{P_\infty}\right) \quad (6)$$

where u_f is the gas velocity, S_L is the laminar burning velocity (0.39 m/s for methane [56]), $Re_L = D_{or} S_L / \nu$ is the Reynolds number based on D_{or} and S_L, and P_i and P_a are the stagnation and ambient pressures, respectively. The U^* values obtained for the experiments analysed here range between 10.6 (for 1 atm) to 12.5 (for 0.6 atm). Thus, the jet flames are at the beginning of the transition regime from buoyant to momentum-dominated flames. In this sense, the non-dimensional expression defined by Lin et al. [57] for buoyant and transition regimes can be applied:

$$D^* / \delta_x = \left(\frac{\dot{Q}}{\rho_\infty c_p T_\infty \sqrt{g}}\right)^{2/5} \Big/ \delta_x \quad (7)$$

where D^* is the characteristic diameter of the fire, δ_x is the cell size, $\dot{Q}$ is the heat release rate, ρ_∞ is the ambient density, c_p is the specific heat of air, T_∞ is the ambient temperature, and g is the gravitational acceleration.

This dimensionless parameter expresses how well the flow field is numerically solved. In order to determine the optimal grid resolution, the flame-geometry descriptors were predicted in the CFD codes by using four different cell sizes, δ_x: 32 mm-cell for $D^*/\delta_x = 4$, 24 mm-cell for $D^*/\delta_x = 8$, 16 mm-cell for $D^*/\delta_x = 12$, and 8 mm-cell for $D^*/\delta_x = 16$. Therefore, a total of 20 fire simulations are performed for each fire code. The dimensionless expression values proposed for mesh sensitivity analysis, D^*/δ_x (ranged from 4 to 16), have been used in previous works for computational simulations of hydrocarbon diffusion flames [44,57].

As observed, the cell sizes calculated are larger than the original exit orifices (3 mm-diameter). Because of that, equivalent nozzle diameters are defined with the same size than the calculated cell. For example, a vertical subsonic jet fire modelled with a $D^*/\delta_x = 12$ is modelled with an equivalent nozzle diameter of 0.016 m and a cell volume of 0.016 x 0.016 x 0.016 m^3. As a consequence, an equivalent mass flow rate, $\dot{m}_{eq} = 0.25\rho_f u_f \pi {D_{eq,n}}^2$, is calculated for each cell size defined and prescribed within the computational simulation.

The cell sizes previously defined have been used in the CFD codes regardless of their capabilities to perform unstructured grid simulations. By this, a better comparison of codes can be achieved on an equal basis (i.e. cell size, fuel reaction, domain, time step, etc.), despite the evident mathematical differences in terms of numerical schemes and sub-models solved, especially in FLACS-Fire. A further investigation analysis could consider unstructured grids or even more refined grids near the nozzle orifice. The results obtained could be then compared against the outcomes found in the current work.

The computational domains modelled in the CFD codes are composed by rectangular and isotropic cells with a volume of 0.6 (Length) x 0.6 (Width) x 1.0 (Height) m^3 for all the simulations performed.

3.4. Simulation outputs

Two dimensional slice files were positioned on the centreline axis of the nozzle orifice to record temperature evolution. Different post-processing tools were used to convert the slice files into spreadsheets containing mean temperature values registered at each cell every 1 second: fds2ascii for FDS, ParaView v5.4 for FireFOAM, and Flowvis v5 for FLACS-Fire. After that, a threshold temperature (T_{th}) was set to perform a flame segmentation process within the CFD domain by comparing the temperature at each cell ($T_{i,j}$) with the defined threshold temperature:

$$I(i,j) = \begin{cases} 1, if\ T_{i,j} \geq T_{th} \\ 0, if\ T_{i,j} < T_{th} \end{cases} \quad (8)$$

where $I(i,j)$ is the segmented image and 1 indicates that the cell is within the flame region, and 0 means that the cell belongs to the background of the image. Cells with $T_{i,j} \geq 600\ K$ were considered as flame [58], while the rest were considered as background. More details about this processing technique can be found in Rengel et al. [44].

4. Results and discussion

4.1. Experimental results

Figure 5 shows instant captures of (a) original images and (b) segmented images obtained during the stationary state of the jet fire experiments. As seen, the shapes and the colours of the jet flames significantly varied according to the ambient pressure. This may be due to the effective amount of oxygen available, which altered the soot formation rate and the chemical reaction rate [59,60].

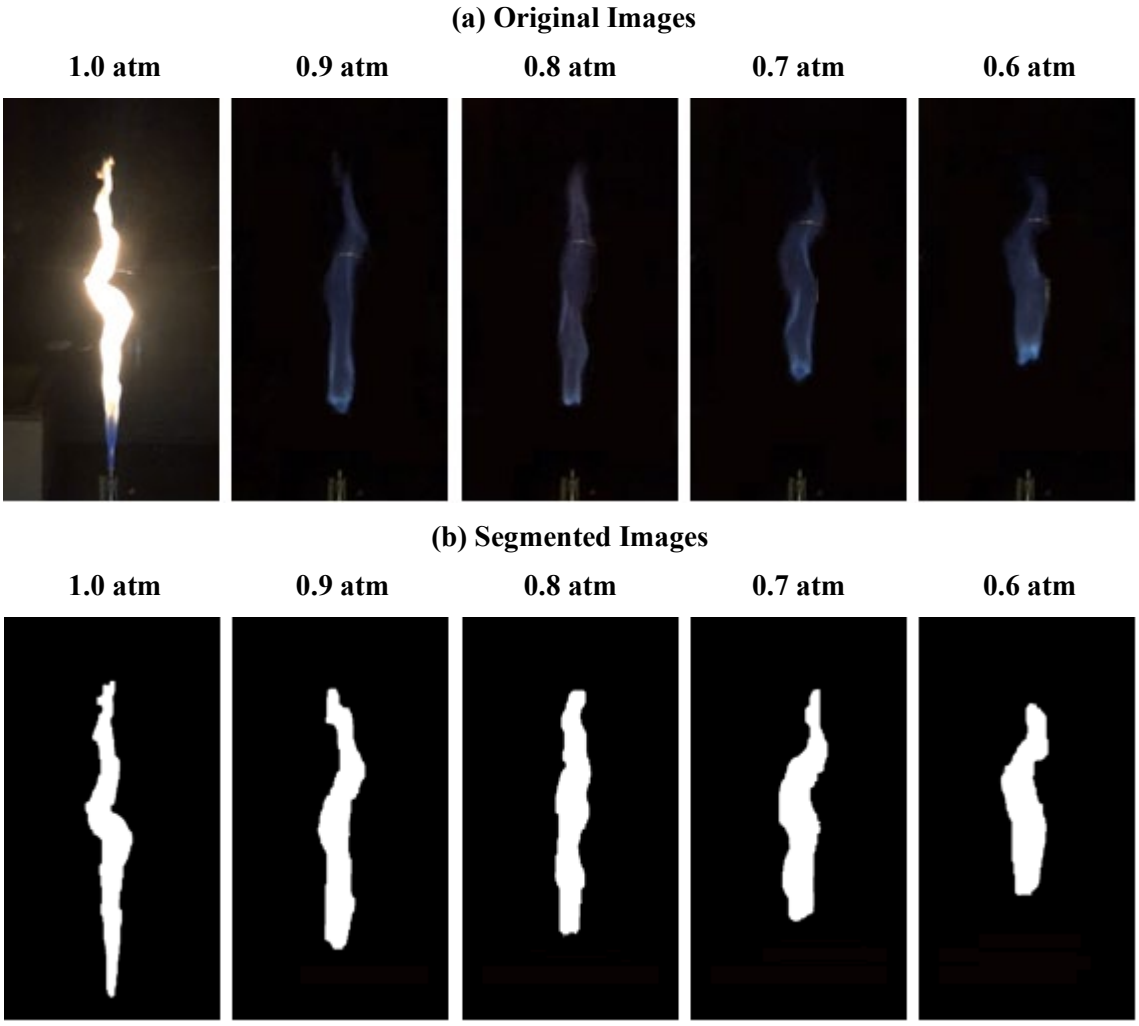

Fig. 5. Instant captures of (a) original and (b) segmented images obtained during the stationary state of the vertical jet fire experiments of methane in normal and sub- atmospheric pressures.

At 1.0 atm, there was sufficient oxygen present near the base of the flame to support the reaction of combustion from the nozzle orifice. As the axial distance from the orifice increased, the flame turned to be more yellow and luminous, indicating the oxidation of the soot particles as a result of an incomplete combustion process [61].

At lower pressures, there was no formation of soot given the lower amount of oxygen particles present in air, hence creating a blue and smaller flame. Indeed, reduced atmospheres lead to premixed flames due to the lower concentration of oxygen molecules and the better fuel/air mixing process.

The mean results of the (a) lift-off distances, (b) radiant flame lengths, and (c) equivalent flame diameters obtained from the image segmentation process are shown in Fig. 6 as a function of the Reynolds number. Vertical error bars indicate the standard deviation of the measurements obtained from the images segmented for each fire experiment. Linear trend lines reveal the

variables evolution. The geometrical parameters are expressed in dimensionless quantities as a function of the nozzle diameter to allow further comparison with other jet fire experiments.

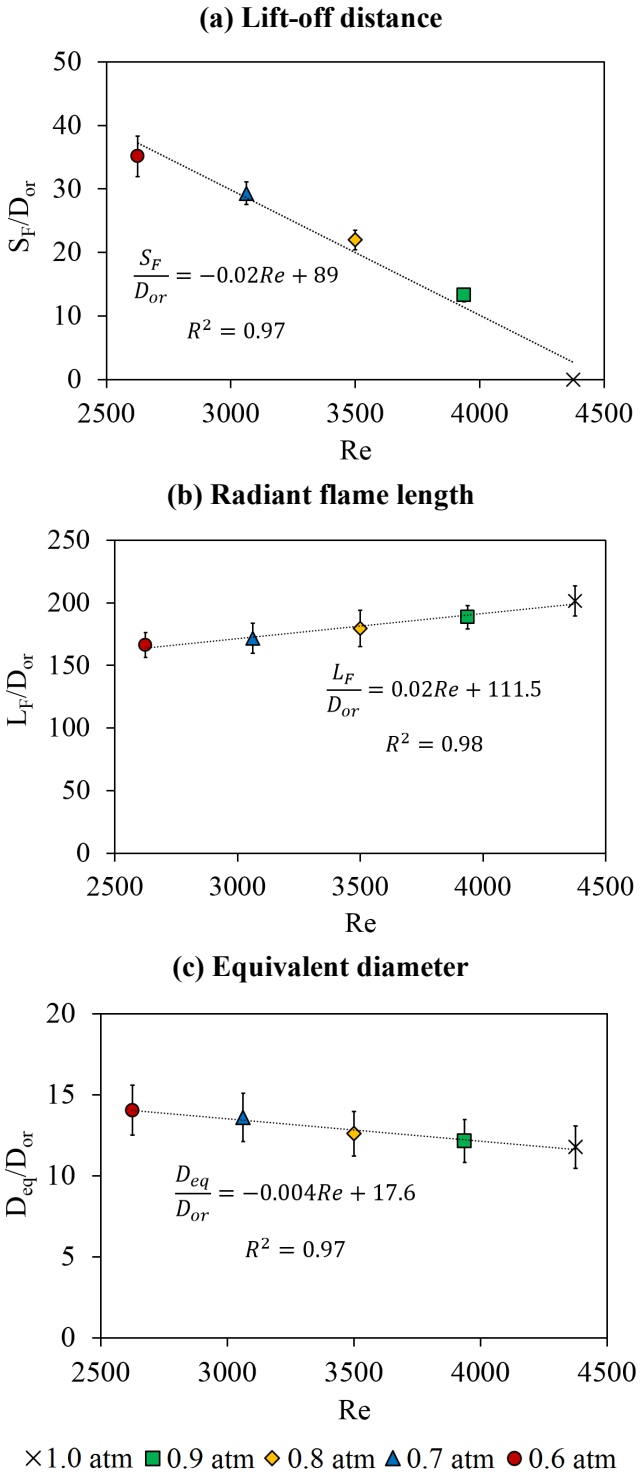

Fig. 6. Mean values of the (a) lift-off distances, (b) radiant flame lengths, and (c) equivalent diameters as a function of the Reynolds number.

The mean lift-off distance varied according to the ambient pressure: the lower the atmospheric pressure, the larger the flameless distances. This occurred due to the high amount of fuel released downstream the orifice that required a significant amount of oxygen molecules, which were not present at reduced pressures. As the methane gas was diluted into the ambient air, its concentration decreased until the fuel-oxidizer mixture was within the flammability limits. A similar tendency

on the lift-off behaviour was found in methane jet fire experiments performed by Zeng et al. [22], who examined laminar flames released from 3 mm-diameter nozzles and ambient pressures ranged from 0.5 atm to 1.0 atm.

The radiant flame length increased with the Reynolds number, whereas the equivalent diameter remained approximately steady (slope of the linear trend = -0.004). Thus, vertical jet flames of methane became thinner as the ambient pressure decreased. Given the opposite behaviour of the lift-off distance and the radiant flame length (note that slopes have the same absolute value), the total flame length (H_F) remained steady regardless the ambient pressure tested. Therefore, the flame always achieves the same total length from the exit orifice and occupies the same area (Fig. 7). These values were found to be $H_F = 200D_{or}$ and $A_F = 3000A_{or}$.

It is worth noting that sooty flames, such as those occurring at 1 atm, are featured with lower temperatures since the radiative fraction is higher than at sub-atmospheric pressures [19,20]. In addition, the radiant flame lengths are larger and closer to the nozzle orifice at 1 atm than at reduced atmospheres. Consequently, in terms of geometrical characteristics, jet flames pose a more hazardous situations at 1 atm than at reduced ones given the greater possibility of flame impingement in adjacent equipment. However, higher thermal fluxes are expected to be emitted in sub-atmospheric pressures.

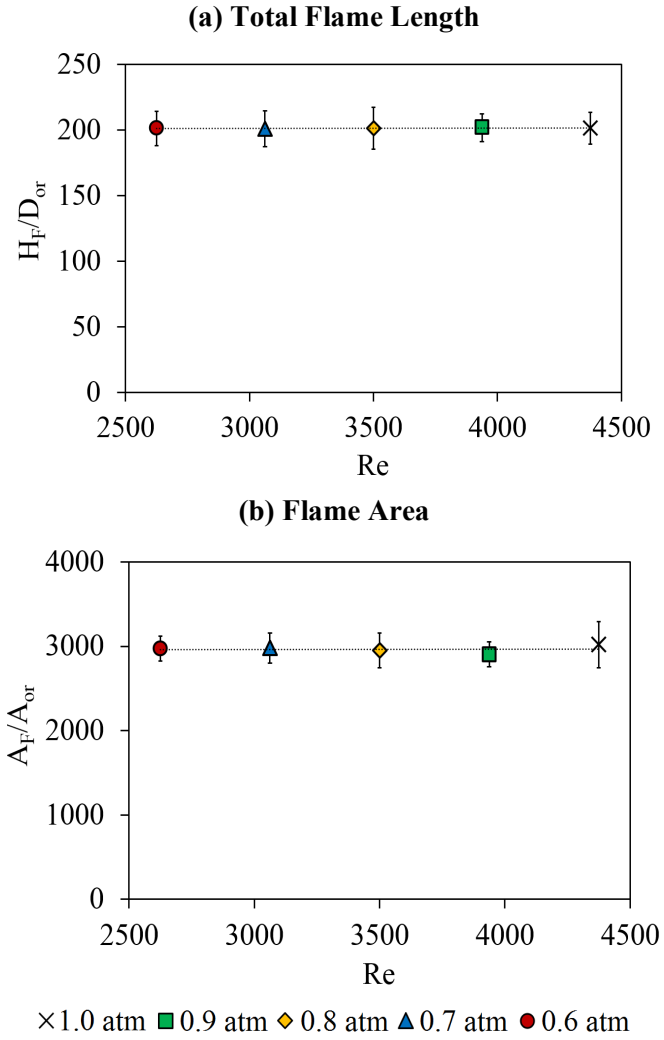

Fig. 7. Mean values of the (a) total flame lengths, and (b) the flame areas as a function of the Reynolds number.

4.2. Modelling results

4.2.1. Qualitative assessment of the predictions

The following scatter plots (Figs. 8 and 9) illustrate the level of agreement reached by the flame-geometry descriptors predicted with the codes using different cell sizes. The solid diagonal line indicates perfect agreement between simulation results and experimental data, while dotted lines and long-dashed lines represent the ± 25 % and ± 50 % prediction error, respectively, with regard to the experimental measurement. Vertical bars represent the standard deviation of the simulation results obtained from the slice files, and the horizontal ones indicate the standard deviation of the experimental measurements. It is worth noting that neither FLACS-Fire nor FireFOAM were able to predict flame temperatures higher than 600 K under cells of 32 mm (results not shown). Therefore, both codes are unable to solve the rate of fuel/oxidant mixing under coarse grids.

Figure 8 shows mean predicted values of the lift-off distances (left) and the radiant flame lengths (right) estimated for different pressures and cell sizes with (a) FDS, (b) FireFOAM, and (c) FLACS-Fire. None of the codes is able to capture the influence of the ambient pressure on the lift-off distances (i.e. a steady trend is generally obtained). This fact may be probably due to the 'mixed is burnt' assumption considered in the EDC combustion model, which immediately ignites the gas fuel entering into the domain simulated. Favrin et al. [62] also pointed out the limitations of computational combustion models to simulate jet fires.

Furthermore, FDS and FLACS-Fire are able to predict the radiant flame lengths with an error estimation lower than 25 % with cells of 8 mm and 16 mm, whereas the error is much pronounced for greater grid sizes. Contrarily, a minimum error estimation of 25 % is achieved in FireFOAM for cell sizes of 24 mm for all the ambient pressures tested. The notable differences on the accuracy of the results obtained with FDS are probably derived from the mathematical approach adopted for the mixing time scales. More complex models, as those implemented in FDS, may contribute to provide higher precision on the flame length estimations.

Figure 9 depicts the mean predicted values of the equivalent diameters (left) and flame surfaces (right) estimated for different pressures and cell sizes with (a) FDS, (b) FireFOAM, and (c) FLACS-Fire. Reasonable agreements on the equivalent diameter are generally obtained with FDS. The mean error estimation is lower than 25 % when the cells are of 24 mm or higher, whereas it is comprised between 25 % and 50 % for smaller cells. Particularly, thinner grids over-predict the equivalent diameter of the jet. This may be due to possible measuring errors during the segmentation process from the video recordings, or from the temperature slice files. Similarly, mean equivalent diameters calculated with FireFOAM provide an average error estimation of 30 % with light differences among the cell sizes simulated. In contrast, greater over-estimations of the equivalent diameters are found in FLACS-Fire, with error estimations much higher than 50 %. This means that the flames predicted in FLACS-Fire are much wider than in reality.

As for the estimation of the flame surface, which corresponds to the projected area with cells having temperatures greater than 600 K, different levels of accuracy are achieved according to the grid sizes and the CFD codes. For example, in FDS the thinner the size of the cells, the greater the surface of the flame estimated. The most accurate predictions are found for cells of 16 mm, while an error estimation of 30 % approximately is found for cells of 8 mm and 24 mm. On the other hand, the best agreement obtained in FireFOAM occurs with cells of 24 mm, which is in accordance with the radiant flame length predictions. Differently, flame surfaces calculated with FLACS-Fire are significantly over-estimated.

The cell size modelled is the parameter that mostly affects the standard deviations found: the coarser the cell size modelled, the less noticeable the error bars found. The negligible variations obtained demonstrate that most of the air/fuel mixing effects on the flame's surfaces are not completely considered; hence leading to more stable flames. This fact may lead to sudden fluctuations of the dependent flame shape parameters, such as the emissive powers or the heat fluxes received at a certain distance from the flame origin.

Apart from the cell size influence, the deviations found also varied in minor way depending on the geometrical parameter estimated. For example, the smallest deviations are found on the flame length's predictions; while the highest one are found in the predictions of the flame areas. This notorious difference, between the error bars found in both measurements, highlights the strong influence of the air entrained into the base and surroundings of the jet flames.

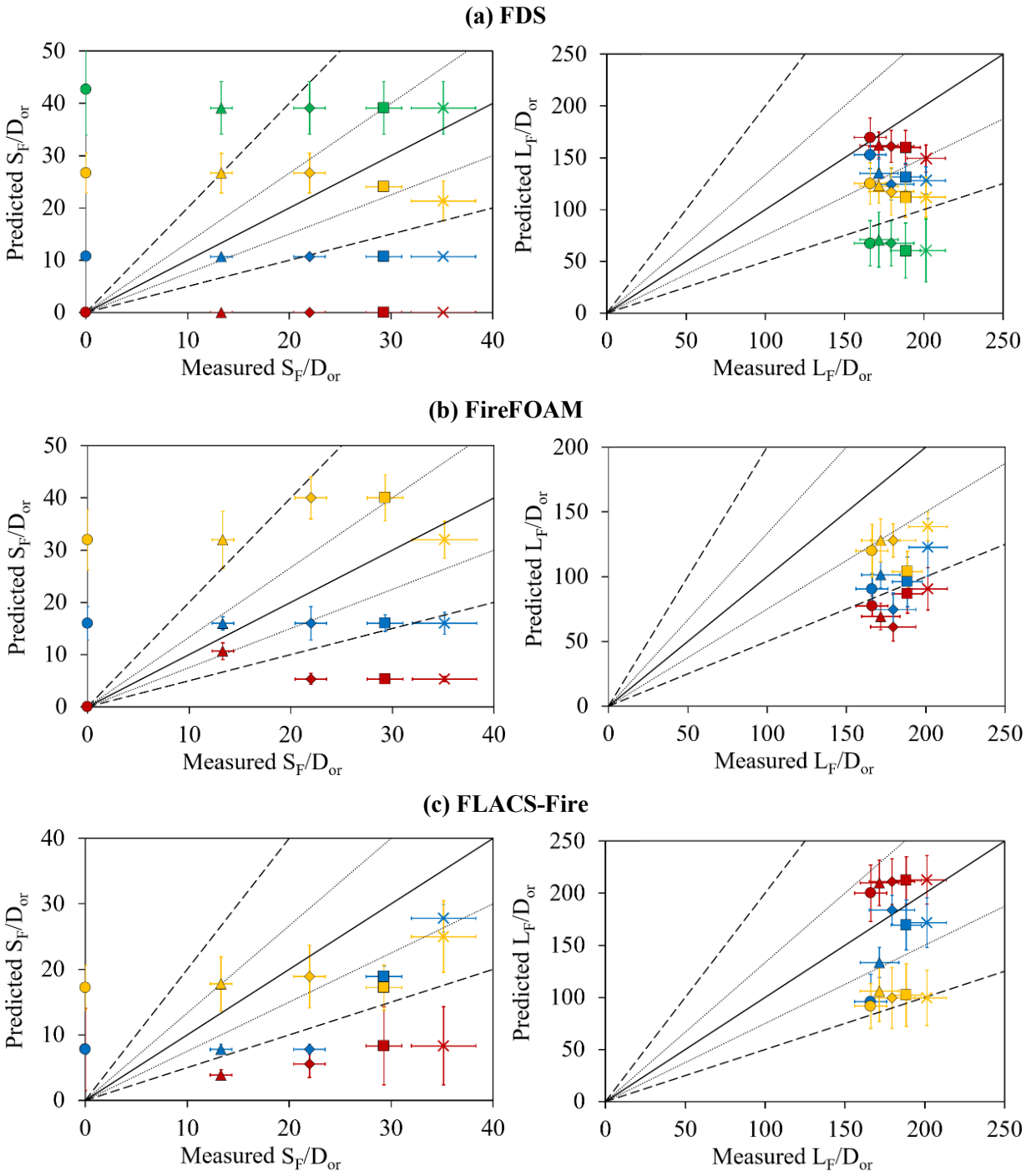

Fig. 8. Predicted values of the mean lift-off distances (left) and the mean radiant flame lengths (right) estimated with (a) FDS, (b) FireFOAM, and (c) FLACS-Fire for the different ambient pressures and cell sizes modelled.

Figure 10 shows instant captures (up) and the corresponding segmented images (down) of jet flames at 0.6 atm (left) and 1.0 atm (right) obtained from the slice files of temperatures set in the CFD codes with a cell size of 16 mm. These images help to understand the tendency of the flame shape obtained with the different computational codes. As previously described and regardless of the ambient pressure, more reasonable predictions (lengths and diameter) are obtained with FDS and FireFOAM, while large flames are found with FLACS-Fire.

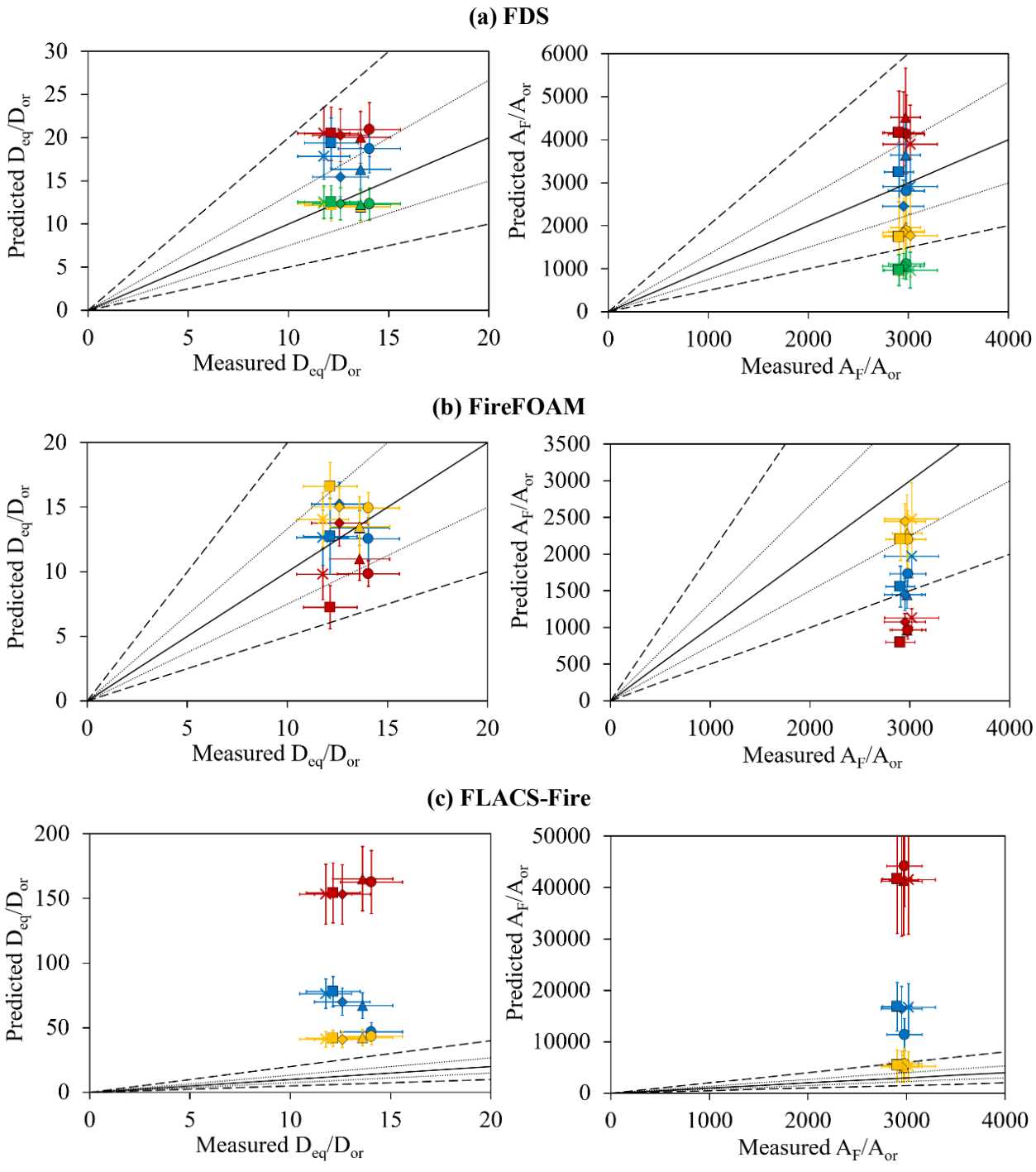

Fig. 9. Predicted values of the mean equivalent diameters (left) and the mean flame surfaces (right) estimated with (a) FDS, (b) FireFOAM, and (c) FLACS-Fire for the different ambient pressures and cell sizes.

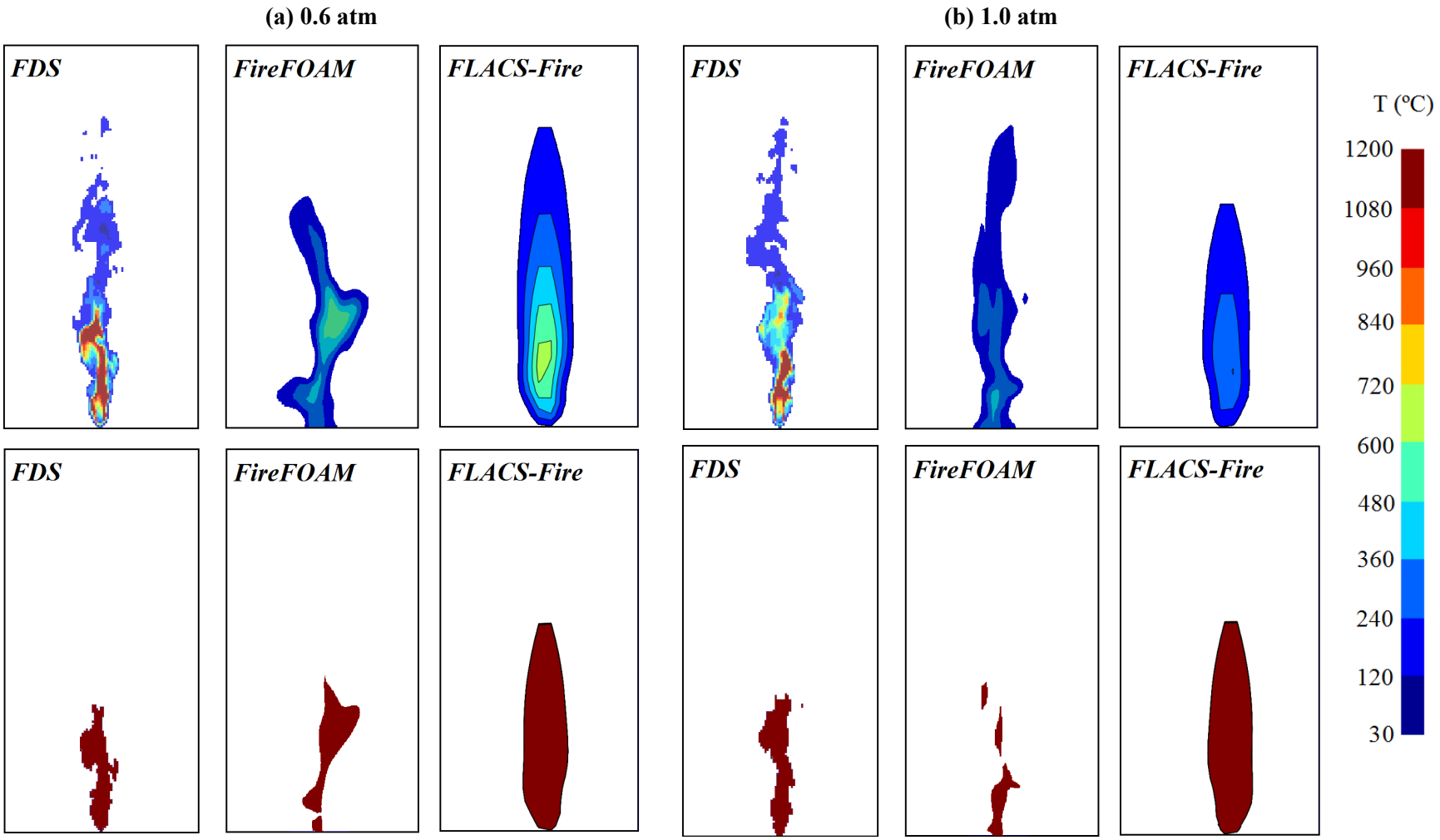

Fig. 10. Instant captures (up) and segmented images (down) of the slice file of temperatures corresponding to the fire scenarios at (a) 0.6 atm and (b) 1.0 atm obtained with FDS, FireFOAM, and FLACS-Fire. Images were taken 30 s after ignition.

4.2.2. Cell size recommendation

Given the numerous qualitative comparisons performed, it is challenging to provide recommendations on the most suitable grids according to the codes, the geometrical variables measured and the atmospheric pressures considered. In addition, two quantitative statistical methods have been used to assess the accuracy of the predictions: the fractional bias (FB) and the normalized mean square error (NMSE). These are expressed as:

$$FB = \frac{1}{n}\sum_1^n 2\frac{X_m - X_p}{X_m + X_p} \tag{9}$$

$$NMSE = \frac{1}{n}\sum_1^n 2\frac{(X_m - X_p)^2}{X_m X_p} \tag{10}$$

where n is the total number of variables considered, X_m and X_p are the variables corresponding to the experimental measurements and simulation predictions, respectively. The FB indicates the under/over estimations of the model results, while the NMSE reflects the relative fit of the model estimations to the experimental data. Even though a perfect model would have FB and NMSE values of 0, the following performance criteria (PC) must be met to define a code as "acceptable": NMSE ≤ 0.5 and -0.3 ≤ FB ≤ 0.3 [63]. Table 3 summarizes the FB and NMSE results obtained for the different codes as a function of the cell sizes and atmospheric pressures. Blue italic values indicate that the metric is within the established performance criteria.

Table 3. FB and NMSE values for the flame-geometry descriptors estimated with the codes as a function of the cell sizes and atmospheric pressures considered. Blue italic values indicate that the metric is within the established performance criteria.

CFD	P_∞ (atm)	δ_x (mm)	S_F		L_F		D_{eq}		A_F	
			FB	*NMSE*	*FB*	*NMSE*	*FB*	*NMSE*	*FB*	*NMSE*
FDS	0.6	8	2.00	1.00	*-0.02*	*0.00*	-0.39	*0.16*	-0,41	*0,18*
		16	1.06	1.59	*0.08*	*0.00*	*-0.28*	*0.08*	*-0,20*	*0,04*
		24	0.49	*0.25*	*0.28*	*0.00*	*0.14*	*0.02*	0.41	*0.18*
		32	*-0.11*	*0.01*	0.84	0.87	*0.13*	*0.02*	0.95	1.15
	0.7	8	2.00	1.00	*0.06*	*0.00*	-0.38	*0.15*	*-0.30*	*0.11*
		16	0.93	1.11	*0.24*	*0.06*	*-0.18*	*0.03*	*0.06*	*0.00*
		24	*0.20*	*0.04*	*0.30*	*0.11*	*0.13*	*0.02*	0.46	*0.22*
		32	*-0.29*	*0.08*	0.83	0.83	*0.10*	*0.01*	0.91	1.06
	0.8	8	2.00	1.00	*0.11*	*0.01*	-0.47	*0.23*	*-0.28*	*0.12*
		16	0.69	0.55	*0.26*	*0.14*	*-0.20*	*0.04*	*0.18*	*0.03*
		24	*-0.19*	*0.04*	0.42	*0.18*	*0.02*	*0.00*	0.46	*0.22*
		32	-0.56	*0.34*	0.91	1.03	*0.02*	*0.00*	0.94	1.14
	0.9	8	2.00	1.00	*0.16*	*0.03*	-0.51	*0.28*	*-0.26*	*0.13*
		16	*0.22*	*0.05*	*0.30*	*0.13*	-0.46	*0.22*	*-0.11*	*0.01*
		24	-0.67	*0.50*	0.51	*0.28*	*0.00*	*0.00*	0.50	*0.27*
		32	-0.98	1.28	1.03	1.44	*-0.03*	*0.00*	1.00	1.34
	1.0	8	2.00	1.00	*0.22*	*0.09*	-0.54	*0.31*	*-0.25*	*0.07*
		16	2.00	1.00	*0.29*	*0.20*	-0.41	*0.18*	*0.04*	*0.00*
		24	2.00	1.00	0.57	*0.35*	*-0.05*	*0.00*	0.52	*0.29*
		32	2.00	1.00	1.07	1.63	*-0.06*	*0.00*	1.03	1.44
FireFOAM	0.6	8	1.47	4.73	0.73	0.61	0.35	*0.13*	1.02	1.39
		16	0.74	0.65	0.59	0.38	*0.11*	*0.01*	0.69	0.54
		24	*0.09*	*0.01*	*0.30*	*0.11*	*-0.06*	*0.00*	*0.26*	*0.07*

CFD	P_∞ (atm)	δ_x (mm)	S_F		L_F		D_{eq}		A_F	
			FB	***NMSE***	***FB***	***NMSE***	***FB***	***NMSE***	***FB***	***NMSE***
	0.7	8	1.38	3.68	0.85	0.88	*0.21*	*0.05*	1.02	1.40
		16	0.59	*0.38*	0.52	*0.28*	*0.01*	*0.00*	0.53	*0.30*
		24	*-0.29*	*0.10*	*0.29*	*0.09*	*0.01*	*0.00*	*0.30*	*0.09*
	0.8	8	1.22	2.36	0.98	1.27	*-0.09*	*0.01*	0.93	*1.11*
		16	0.31	*0.10*	0.82	0.82	*-0.19*	*0.04*	0.68	*0.43*
		24	-0.58	*0.37*	*0.23*	*0.12*	*-0.17*	*0.03*	*0.19*	*0.04*
	0.9	8	*0.22*	*0.05*	0.74	0.63	0.50	*0.27*	1.14	1.91
		16	*-0.18*	*0.03*	0.65	*0.47*	*-0.05*	*0.00*	0.60	*0.40*
		24	-0.82	0.82	*0.28*	*0.36*	*-0.27*	*0.10*	*0.28*	*0.08*
	1.0	8	2.00	1.00	0.76	*0.67*	*0.18*	*0.03*	0.91	1.04
		16	2.00	1.00	0.49	*0.25*	*-0.07*	*0.01*	0.42	*0.18*
		24	2.00	1.00	*0.30*	*0.14*	*-0.18*	*0.03*	*0.20*	*0.04*
FLACS-Fire	0.6	8	1.23	2.45	*-0.18*	*0.03*	-1.68	9.66	-1.73	12.01
		16	*0.23*	*0.06*	0.53	*0.31*	-1.08	1.64	-0.63	0.45
		24	*0.30*	*0.12*	0.58	*0.36*	-1.02	1.42	-0.52	0.29
	0.7	8	1.11	1.80	*-0.20*	*0.04*	-1.70	10.22	-1.75	12.89
		16	0.43	*0.20*	*0.25*	*0.06*	-1.33	3.13	-1.17	2.08
		24	*0.28*	*0.29*	0.47	*0.24*	-1.03	1.44	-0.63	0.44
	0.8	8	1.19	2.21	*-0.16*	*0.03*	-1.70	10.24	-1.73	12.03
		16	0.95	1.18	*-0.02*	*0.00*	-1.39	3.74	-1.39	3.74
		24	*0.15*	*0.02*	0.57	*0.36*	-1.06	1.55	-0.55	0.33
	0.9	8	1.10	1.72	*-0.12*	*0.01*	-1.71	10.78	-1.74	12.41
		16	0.53	*0.30*	*0.11*	*0.01*	-1.46	4.58	-1.41	3.97
		24	*-0.29*	*0.08*	0.59	*0.39*	-1.10	1.74	-0.61	*0.41*
	1.0	8	2.00	1.00	*-0.05*	*0.00*	-1.71	11.11	-1.73	11.83
		16	2.00	1.00	*0.16*	*0.03*	-1.47	4.64	-1.39	3.71
		24	2.00	1.00	0.68	0.52	-1.11	1.78	-0.53	*0.30*

Apart from the lift-off distance, the rest of geometrical parameters estimated with FDS meet the PC in more than the 50 % of the cases. In particular, the most accurate results are obtained with a cell size of 16 mm ($D^*/\delta_x \approx 12$). Likewise, a similar agreement between predictions and measurements is determined with FireFOAM. Among the geometrical variables calculated, the mean equivalent diameter is the parameter simulated with greater accuracy as a result of the equilibrium reached between the over-estimated flame lengths and flame surfaces. The best agreement between simulation results and experiments was reached for grids of 24 mm ($D^*/\delta_x \approx 8$). On the other hand, the statistical measurements do not meet the PC defined in most of the predictions performed with FLACS-Fire. The only geometrical variable that can be reasonably estimated is the radiant flame length for cell sizes between 8 mm to 16 mm ($12 \leq D^*/\delta_x \leq 16$). The accurate predictions found with FDS and FireFOAM codes point out their capacity to estimate the flame shapes of vertical methane jet fires at different ambient pressures. Indeed, these codes would be recommended to be used to reasonably determine the safety measures required to prevent major accidents in oil and gas industries derived from methane jet fire accidents.

4.2.3. Soot yield influence

Experiments have shown that different flame colours and shapes can be observed depending on the ambient pressure. This may be due to differences in combustion efficiency. In this regard, the soot yield fraction prescribed in CFD codes for methane (0.7 %) (very low compared to other hydrocarbon fuels, such as propane (9.0 %) or heptane (12.9 %)), which directly affects the products of combustion formed (Eq. 4), may have a direct influence on the estimated flame shapes. In order to assess the influence of this parameter on the flame shapes, six simulations have been run in FDS with cell sizes of 16 mm (as it was previously observed that it is a good cell size for most of the geometry descriptors). Specifically, different soot yield fractions have been tested in jet flames at 0.7 atm and 1.0 atm: 0.7 %, 0.5 %, 0.3 %, and no soot at all.

Table 4 shows the estimations of the radiant flame lengths, equivalent diameters, and flame surfaces obtained with FDS for different soot yield fractions and ambient pressures of 0.7 atm and 1.0 atm. As observed, the flame shape estimations are very similar value regardless of the soot yield fractions and the ambient pressure defined. Thus, its influence on the flame shape predictions is negligible.

Table 4. Flame shapes predicted in FDS with cell sizes of 16 mm and different soot yield fractions.

Soot yield fractions	P_∞ (atm)	L_F (m)	D_{eq} (m)	A_F (m^2)
0.7 %	0.7	0.41	0.047	0.018
	1.0	0.42	0.050	0.021
0.5 %	0.7	0.41	0.048	0.020
	1.0	0.42	0.050	0.022
0.3 %	0.7	0.44	0.052	0.023
	1.0	0.44	0.051	0.022
0.0 %	0.7	0.45	0.051	0.023
	1.0	0.42	0.047	0.019

5. Conclusions

Vertical methane subsonic jet fire experiments were studied to assess the flame-geometry descriptors at different ambient pressures: 1.0 atm, 0.9 atm, 0.8 atm, 0.7 atm, and 0.6 atm, which would correspond to different heights above the sea level. Different flame shapes and luminosities were obtained as the ambient pressure decreased. This occurred as a result of the decreasing effective amount of oxygen available in the ambient air, which, according to the literature, affects the soot formation rate and the chemical reaction between the fuel and the oxidizer. At 1.0 atm sufficient oxygen was present near the flame, hence promoting the oxidation of soot and allowing the reaction of combustion from the nozzle orifice. In contrast, a lack of oxygen hindered the soot formation and the fuel/air mixture downstream the orifice. In general, the lower the ambient pressure, the larger the lift-off distance and the shorter the radiant flame length. However, the total flame length remained essentially constant in spite of the pressure variations. Linear correlations based on the Reynolds number were obtained from the experimental data.

Furthermore, the predictive capabilities of FDS, FireFOAM and FLACS-Fire were assessed when determining the geometrical parameters of the methane jet fires experiments. Four different grids were selected for each methane jet fire experiment: 8 mm, 16 mm, 24 mm, and 32 mm. A qualitative and quantitative analysis of the predictions was carried out to determine the performance of each code. Reasonable predictions of the radiant flame lengths, equivalent diameters, and flame surfaces were usually found with FDS and FireFOAM. Nevertheless, more precise outcomes were obtained with FDS due to the more detailed mixing scale times. The highest agreement occurred when the dimensionless D^*/δ_x correlation was of 12 and 8 for FDS

and FireFOAM simulations, respectively. On the other hand, a considerable lack of agreement of the equivalent diameters and flame areas was obtained with FLACS-Fire in spite of the reasonable flame length estimations. In addition, the soot yield fraction had a negligible influence on the flame shape predictions.

This paper has shown the impact of ambient pressures on the flame shapes of vertical jet fires. Likewise, it has revealed the great potential of CFD codes to assess their geometrical features. In particular, FDS is found to be the most suitable CFD code to estimate the flame-geometry descriptors of methane jet fires at reduced-pressure atmospheres. Further work is needed to study different fuels, ambient conditions (i.e. wind and temperature), and to analyse their effects on other fire variables, such as temperature contours and radiative heat fluxes.

ACKNOWLEDGMENTS

This research was partially funded by the Spanish Ministry of Economy and Competitiveness (project CTM2014-57448-R and CTQ2017-85990-R, co-financed with FEDER funds). A.P. gratefully acknowledges the financial support of the Royal Society in the form of a Postdoctoral Newton International Fellowship.

REFERENCES

[1] Palazzi E, Fabiano B. Analytical modelling of hydrocarbon pool fires: Conservative evaluation of flame temperature and thermal power. Process Saf Environ Prot 2012;90:121–8. https://doi.org/10.1016/j.psep.2011.06.009.

[2] Planas-Cuchi E, Montiel H, Casal J. A survey of the origin, type and consequences of fire accidents in process plants and in the transportation of hazardous materials. Process Saf Environ Prot 1997;75:3–8. https://doi.org/10.1205/095758297528706.

[3] Lowesmith BJ, Hankinson G, Acton MR, Chamberlain G. An overview of the nature of hydrocarbon jet fire hazards in the oil and gas industry and a simplified spproach to assessing the hazards. Process Saf Environ Prot 2007;85:207–20. https://doi.org/10.1205/psep06038.

[4] Gómez-Mares M, Zárate L, Casal J. Jet fires and the domino effect. Fire Saf J 2008;43:583–8. https://doi.org/10.1016/j.firesaf.2008.01.002.

[5] Casal J, Gómez-Mares M, Muñoz M, Palacios A. Jet fires: a “minor” fire hazard? Chem Eng Trans 2012;26:13–20. https://doi.org/10.3303/CET1226003.

[6] Peter N, Williams FA. Lift-off characteristics of turbulent jet diffusion flames. Am Inst Aeronaut Astronaut J 1983;21:423–9.

[7] Sonju OK, Hustad J. An experimental study of turbulent jet diffusion flames. Nor Marit Res 1984;4:2–11.

[8] Gore JP. A Theoretical and Experimental Study of Turbulent Jet Flame Radiation. The Pennsylvania State University, University Park, 1986.

[9] McCaffrey BJ. Momentum diffusion flame characteristics and the effects of water spray. Combust Sci Technol 1989;63:315–35. https://doi.org/10.1080/00102208908947134.

[10] Rokke NA, Hustad JE, Sonju OK. A study of partially premixed unconfined propane flames. Combust Flame 1994;97:88–106. https://doi.org/10.1016/0010-2180(94)90118-X.

[11] Sugawa O, Sakai K. Flame length and width produced by ejected propane gas fuel from a pipe. Fire Sci Technol 1997;17:55–63. https://doi.org/10.3210/fst.17.55.

[12] Costa M, Parente C, Santos A. Nitrogen oxides emissions from buoyancy and momentum

controlled turbulent methane jet diffusion flames. Exp Therm Fluid Sci 2004;28:729–34. https://doi.org/10.1016/j.expthermflusci.2003.12.010.

[13] Santos A, Costa M. Reexamination of the scaling laws for NOxemissions from hydrocarbon turbulent jet diffusion flames. Combust Flame 2005;142:160–9. https://doi.org/10.1016/j.combustflame.2005.03.004.

[14] Kiran DY, Mishra DP. Experimental studies of flame stability and emission characteristics of simple LPG jet diffusion flame. Fuel 2007;86:1545–51. https://doi.org/10.1016/j.fuel.2006.10.027.

[15] Gómez-Mares M, Muñoz M, Casal J. Axial temperature distribution in vertical jet fires. J Hazard Mater 2009;172:54–60. https://doi.org/10.1016/j.jhazmat.2009.06.136.

[16] Palacios A, Casal J. Assessment of the shape of vertical jet fires. Fuel 2011;90:824–33. https://doi.org/10.1016/j.fuel.2010.09.048.

[17] Palacios A, Muñoz M, Darbra RM, Casal J. Thermal radiation from vertical jet fires. Fire Saf J 2012;51:93–101. https://doi.org/10.1016/j.firesaf.2012.03.006.

[18] Hu L, Wang Q, Delichatsios M, Tang F, Zhang X, Lu S. Flame height and lift-off of turbulent buoyant jet diffusion flames in a reduced pressure atmosphere. Fuel 2013;109:234–40. https://doi.org/10.1016/j.fuel.2012.12.050.

[19] Hu LH, Wang Q, Tang F, Delichatsios M, Zhang XC. Axial temperature profile in vertical buoyant turbulent jet fire in a reduced pressure atmosphere. Fuel 2013;106:779–86. https://doi.org/10.1016/j.fuel.2012.10.051.

[20] Hu L, Wang Q, Delichatsios M, Lu S, Tang F. Flame radiation fraction behaviors of sooty buoyant turbulent jet diffusion flames in reduced- and normal atmospheric pressures and a global correlation with Reynolds number. Fuel 2014;116:781–6. https://doi.org/10.1016/j.fuel.2013.08.059.

[21] Hu L, Zhang X, Wang Q, Palacios A. Flame size and volumetric heat release rate of turbulent buoyant jet diffusion flames in normal- and a sub-atmospheric pressure. Fuel 2015;150:278–87. https://doi.org/10.1016/j.fuel.2015.01.081.

[22] Zeng Y, Fang J, Wang J, Li J, Tu R, Zhang Y. Momentum-dominated methane jet flame at sub-atmospheric pressure. Procedia Eng 2013;62:924–31. https://doi.org/10.1016/j.proeng.2013.08.144.

[23] Wang Q, Hu L, Zhang M, Tang F, Zhang X, Lu S. Lift-off of jet diffusion flame in sub-atmospheric pressures: An experimental investigation and interpretation based on laminar flame speed. Combust Flame 2014;161:1125–30. https://doi.org/10.1016/j.combustflame.2013.10.021.

[24] Bang S, Lee BJ, Chung SH. Effect of pressure on the characteristics of lifted flames. Proc Combust Inst 2019;37:2013–20. https://doi.org/10.1016/j.proci.2018.06.094.

[25] Structurae. International Database and Gallery of Structures. Troll A Platform n.d. https://structurae.net/structures/troll-a-platform (accessed May 23, 2019).

[26] Hydrocarbons Technology. Blake Oil Field Exploitation n.d. https://www.hydrocarbons-technology.com/projects/blake/ (accessed May 23, 2019).

[27] Industry About. Gate - Maasvlakte LNG Plant 2016. https://www.industryabout.com/country-territories-3/1643-netherlands/oil-and-gas/24083-gate-maasvlakte-lng-plant (accessed May 23, 2019).

[28] Industry About. Permian Basin Oil Field 2017. https://www.industryabout.com/country-territories-3/1057-usa/oil-and-gas/41280-permian-basin-oil-field (accessed May 23,

2019).

[29] Industry About. F'Kirina Gas Power Plant 2014. https://www.industryabout.com/country-territories-3/1181-algeria/fossil-fuels-energy/15909-f-kirina-gas-power-plant.

[30] U.S. Energy Information Administration (EIA). Natural Gas Production/Consumption - 2015 2018. https://www.eia.gov/beta/international/.

[31] Dadashzadeh M, Khan F, Hawboldt K, Amyotte P. An integrated approach for fire and explosion consequence modelling. Fire Saf J 2013;61:324–37. https://doi.org/10.1016/j.firesaf.2013.09.015.

[32] Jang CB, Choi SW. Simulation and damage analysis of an accidental jet fire in a high-pressure compressed pump shelter. Saf Health Work 2017;8:42–8. https://doi.org/10.1016/j.shaw.2016.06.005.

[33] Rajendram A, Khan F, Garaniya V. Modelling of fire risks in an offshore facility. Fire Saf J 2015;71:79–85. https://doi.org/10.1016/j.firesaf.2014.11.019.

[34] Sun L, Yan H, Liu S, Bai Y. Load characteristics in process modules of offshore platforms under jet fire: The numerical study. J Loss Prev Process Ind 2017;47:29–40. https://doi.org/10.1016/j.jlp.2017.02.018.

[35] Wang C, Guo J. Computer simulation of liquid jet fire with various injection conditions. Procedia Eng 2011;15:3942–7. https://doi.org/10.1016/j.proeng.2011.08.738.

[36] Mok WK, Chow WK, Kong H. "Verification and validation" computational fluid dynamics in fire. Int J Archit Sci 2004;5:58–67.

[37] Higher Peak Altitude Training. The effective amount of oxygen at different altitudes n.d. https://www.higherpeak.com/altitudechart.html# (accessed February 15, 2019).

[38] McGuinness K, O'Connor NE. A comparative evaluation of interactive segmentation algorithms. Pattern Recognit 2010;43:434–44. https://doi.org/10.1016/j.patcog.2009.03.008.

[39] Adamek T. Using contour information and segmentation for object registration modeling and retrieval. Dubin City University, 2006.

[40] Ferreira T, Rasband W. ImageJ user guide. 2012. https://doi.org/10.1038/nmeth.2019.

[41] McGrattan K, Hostikka S, McDermott R, Floyd J, Vanella M, Weinschenk C, et al. Fire dynamics simulator user's guide. 2017. https://doi.org/10.6028/NIST.SP.1019.

[42] Li YZ, Huang C, Anderson J, Svensson R, Ingason H, Husted B, et al. Verification , validation and evaluation of FireFOAM as a tool for performance design 2017:84.

[43] Gexcon AS. FLACS v10.7 user's manual. 2017.

[44] Rengel B, Mata C, Pastor E, Casal J, Planas E. A priori validation of CFD modelling of hydrocarbon pool fires. J Loss Prev Process Ind 2018;56:18–31. https://doi.org/10.1016/j.jlp.2018.08.002.

[45] Maragkos G, Rauwoens P, Wang Y, Merci B. Large eddy simulations of the flow in the near-field region of a turbulent buoyant helium plume. Flow, Turbul Combust 2013;90:511–43. https://doi.org/10.1007/s10494-012-9437-5.

[46] Kent JH. A quantitative relationship between soot yield and smoke point measurements. Combust Flame 1986;63:349–58. https://doi.org/10.1016/0010-2180(86)90004-0.

[47] Jones WP, Launder B. The prediction of laminarization with a two-equation model of turbulence. Int J Heat Mass Transf 1972;15:301–14. https://doi.org/10.1016/0017-

9310(72)90076-2.

[48] Smagorinsky J. General circulation experiments with the primitive equations. I: The basic experiment. Mon Weather Rev 1963;91:99–165.

[49] McGrattan K, Miles S. Modeling fires using computational fluid dynamics (CFD). In: Hurley M, editor. SFPE Handb. Fire Prot. Eng., 2016, p. 1034–65. https://doi.org/10.1007/978-1-4939-2565-0.

[50] Magnussen B, Hjertager B. On mathematical modeling of turbulent combustion with special emphasis on soot formation and combustion. Symp Combust 1977;16:719–29. https://doi.org/10.1016/S0082-0784(77)80366-4.

[51] Maragkos B, Merci B. Large eddy simulations of CH4 fire plumes. Flow Turbul Combust 2017:239–78. https://doi.org/10.1007/s10494-017-9803-4.

[52] Maragkos G, Beji T, Merci B. Advances in modelling in CFD simulations of turbulent gaseous pool fires. Combust Flame 2017;181:22–38. https://doi.org/10.1016/j.combustflame.2017.03.012.

[53] McDermott R, McGrattan K, Floyd J. A simple reaction time scale for under-resolved fire dynamics. Fire Saf. Sci. - Proc. 10th Int. Symp., 2011, p. 809–20. https://doi.org/10.3801/IAFSS.FSS.10-809.

[54] Miralles A, Ramos M, Pastor E, Planas E. The effect of the computational grid size on the prediction of a flammable cloud. Proc. ASME 2014 33rd Int. Conf. Ocean. Offshore Arct. Eng., 2014, p. 1–8. https://doi.org/10.1115/OMAE2014-24587.

[55] Bradley D, Gaskell PH, Gu X, Palacios A. Jet flame heights, lift-off distances, and mean flame surface density for extensive ranges of fuels and flow rates. Combust Flame 2016;164:400–9. https://doi.org/10.1016/j.combustflame.2015.09.009.

[56] Vagelopoulos CM, Egolfopoulos FN, Law CK. Further considerations on the determination of laminar flame speeds with the counterflow twin-flame technique. Symp Combust 1995;25:1341–7. https://doi.org/10.1016/S0082-0784(06)80776-9.

[57] Lin C, Ferng Y, Hsu W, Hua NT. Investigations on the characteristics of radiative heat transfer in liquid pool fires. Fire Technol 2010;46:321–45. https://doi.org/10.1007/s10694-008-0071-7.

[58] McCaffrey B. Purely buoyant diffusion flames: some experimental results (NBSIR 791910). Washington DC: 1979.

[59] Joo PH, Charest MRJ, Groth CPT, Gülder ÖL. Comparison of structures of laminar methane-oxygen and methane-air diffusion flames from atmospheric to 60atm. Combust Flame 2013;160:1990–8. https://doi.org/10.1016/j.combustflame.2013.04.030.

[60] Lee KO, Megaridis CM, Zelepouga S, Saveliev A V, Kennedy LA, Charon O, et al. Soot formation effects of oxygen concentration in the oxidizer stream of laminar coannular nonpremixed methane air flames. Combust Flame 2000;121:323–33.

[61] Flower WL, Bowman CT. Soot production in axisymmetric laminar diffusion flames at pressures from one to ten atmospheres. Symp Combust 1988;21:1115–24. https://doi.org/10.1016/S0082-0784(88)80342-4.

[62] Favrin S, Busini V, Rota R, Derudi M. Practical LES modelling of jet fires: Issues and challenges. Chem Eng Trans 2018;67:259–64. https://doi.org/10.3303/CET1867044.

[63] Hanna SR, Hansen OR, Dharmavaram S. FLACS CFD air quality model performance evaluation with Kit Fox, MUST, Prairie Grass, and EMU observations. Atmos Environ 2004;38:4675–87. https://doi.org/10.1016/j.atmosenv.2004.05.041.